Dzyaloshinskii–Moriya-like interaction in ferroelectrics and antiferroelectrics

Hong Jian Zhao [1], Peng Chen [1✉], Sergey Prosandeev[1], Sergey Artyukhin[2] and Laurent Bellaiche [1✉]

The Dzyaloshinskii–Moriya interaction (DMI) between two magnetic moments $\mathbf{m}_i$ and $\mathbf{m}_j$ is of the form $\mathbf{D}_{ij} \cdot (\mathbf{m}_i \times \mathbf{m}_j)$. It originates from spin–orbit coupling, and is at the heart of fascinating phenomena involving non-collinear magnetism, such as magnetic topological defects (for example, skyrmions) as well as spin–orbit torques and magnetically driven ferroelectricity, that are of significant fundamental and technological interest. In sharp contrast, its electric counterpart, which is an electric DMI characterized by its $\mathbf{D}'_{ij}$ strength and describing an interaction between two polar displacements $\mathbf{u}_i$ and $\mathbf{u}_j$, has rarely been considered, despite the striking possibility that it could also generate new features associated with non-collinear patterns of electric dipoles. Here we report first-principles simulations combined with group theoretical symmetry analysis which not only demonstrate that electric DMI does exist and has a one-to-one correspondence with its magnetic analogue, but also reveals a physical source for it. These findings can be used to explain and/or design phenomena of possible technological importance in ferroelectrics and multiferroics.

The magnetic Dzyaloshinskii–Moriya interaction (DMI)—arising from spin–orbit coupling between $\mathbf{m}_i$ and $\mathbf{m}_j$ pairs of dipole moments via $H_{DM} = \mathbf{D}_{ij} \cdot (\mathbf{m}_i \times \mathbf{m}_j)$ (refs. [1,2])—is a key factor driving various fascinating phenomena, including non-collinear magnetism (for example, magnetic topological defects such as skyrmions[3–5], vortices[6,7], merons[5,8,9], as well as spin–orbit torques[10]) and magnetically driven ferroelectricity[11,12], that are of great fundamental and technological interest. However, the electric DMI ($\mathbf{D}'_{ij}$) coupling the polar displacements $\mathbf{u}_i$ and $\mathbf{u}_j$, which is the counterpart of magnetic DMI, has rarely been evoked, even though it can also generate new features associated with non-collinear electric dipolar patterns and thus may, for example, also lead to a revisitation or generalization of the laws of electricity and magnetism[13–27]. It is not even clear whether or not an electric DMI exists, although, based solely on symmetry arguments, its existence has been recently hinted[28]. In fact, the electric DMI is usually thought to have no physical grounds, unlike spin–orbit coupling for the magnetic DMI[19]. Here we use first-principles simulations and group theoretical symmetry analysis to investigate whether or not the electric DMI exists. In particular, we not only provide evidence that the electric DMI does exist but also reveal a physical source for it. By investigating the well-known class of materials formed by ABO_3 perovskites, we obtained invariants giving rise to non-collinear (anti)ferroelectricity that suggest a one-to-one correspondence between $\mathbf{D}_{ij}$ and $\mathbf{D}'_{ij}$. We also identified the underlying factors governing such non-collinear alignment of electric dipoles.

Non-collinear magnetism in perovskites driven by magnetic DMI

Let us focus on ABO_3 perovskites and start by recalling that recent works have suggested that a specific magnetic DMI can occur there, involving the tilting of oxygen octahedra (Supplementary Discussion I)[29,30]. Technically, such a DMI can, for example, result in an energy given by $\Delta E \propto \boldsymbol{\omega}^R \cdot (\mathbf{G} \times \mathbf{F})$, where $\boldsymbol{\omega}^R$ is the anti-phase tilting of the BO_6 octahedra and $\mathbf{F}$ and $\mathbf{G}$ are the ferromagnetic (Γ point) and G-type antiferromagnetic (R point) vectors,

respectively[29,30]. Note that the $\mathbf{K}$ vectors and the corresponding modulations are defined in Supplementary Table I. This proposed spin–orbit-driven energy explains in a simple and straightforward way the spin-canting-driven weak ferromagnetism superimposed on the dominating G-type antiferromagnetism in various types of materials including rare-earth orthoferrites[31] and other transition-metal-based perovskites[32], such as chromites, manganates, titanates and halides.

Mechanisms for non-collinear dipole patterns

Our basic starting idea is to search for electric DMIs in ABO_3 perovskites that are also mediated by oxygen octahedral tiltings. We first employ group theory to obtain trilinear coupled invariants of the form $\sum_{\alpha\beta\gamma} \epsilon_{\alpha\beta\gamma} \omega_\alpha Q_{1,\beta} Q_{2,\gamma}$, involving ω_α (in-phase ω^M or anti-phase ω^R tiltings along the α-Cartesian direction) as well as $Q_{1,\beta}$ and $Q_{2,\gamma}$, which are two kinds of ferroelectric or antiferroelectric motions for A or B ions along the β and γ directions, respectively. $\epsilon_{\alpha\beta\gamma}$ is the Levi–Civita symbol. As summarized in Table 1 and sketched in Fig. 1, we have discovered eight such possible couplings with α, β and γ being different from each other, which we denote by E_i ($i=1$–8). We also found four additional couplings (denoted by E_i with $i=9$–12) of the form $\sum_{\alpha\beta\gamma} \epsilon_{\alpha\beta\gamma} \omega_\alpha Q_{1,\delta} Q_{2,\delta'}$ but with (δ, δ') being (β,α), (α,β), (γ,α) or (α,γ)—that is, for which one subscript of a Q mode is identical to that of the pseudo-vector characterizing the tilting of the oxygen octahedra. These 12 mechanisms can be linked with electric DMIs, and thus can generate non-collinear patterns of electric dipoles. Six other couplings (denoted as E_i with $i=13$–18) were discovered as byproducts (Supplementary Table II) and have the analytical form $\sum_{\alpha\beta\gamma} \epsilon_{\alpha\beta\gamma} \omega_\alpha Q_{1,\beta} Q_{2,\beta}$—that is, the index of the two Q modes is identical. Note that in Table 1, as well throughout the manuscript and the Supplementary Information, the quantity d_α^K is defined and widely used to denote the symmetrized displacements (along the α direction) within the d ($d=A$ or B) sublattice and associated with a particular K-point of the five-atom cubic first Brillouin zone. More specifically, d_α^K is given by $\frac{1}{N}\sum_{lmn} e^{(i\mathbf{K}\cdot\mathbf{R}_{lmn})} r_{lmn,\alpha}^d$, where $r_{lmn,\alpha}^d$ denotes the displacement along the α direction of the ion initially located in

Table 1 | The 12 possible trilinear mechanisms for the electric DMI in ABO_3 perovskites

$E_1 \propto \epsilon_{\alpha\beta\gamma}\omega_\alpha^R B_\beta^R B_\gamma^\Gamma$	$E_2 \propto \epsilon_{\alpha\beta\gamma}\omega_\alpha^R B_\beta^{M_\gamma} B_\gamma^{X_\gamma}$	$E_3 \propto \epsilon_{\alpha\beta\gamma}\omega_\alpha^R B_\beta^{M_\beta} B_\gamma^{X_\beta}$	$E_4 \propto \epsilon_{\alpha\beta\gamma}\omega_\alpha^R B_\beta^{M_\alpha} B_\gamma^{X_\alpha}$
$(\underline{\omega_z^R B_x^R B_y^\Gamma} - \omega_z^R B_y^R B_x^\Gamma)$	$(\omega_z^R B_x^{M_y} B_y^{X_y} - \underline{\omega_z^R B_y^{M_x} B_x^{X_x}})$	$(\omega_z^R B_x^{M_x} B_y^{X_x} - \underline{\omega_z^R B_y^{M_y} B_x^{X_y}})$	$(\omega_z^R B_x^{M_z} B_y^{X_z} - \underline{\omega_z^R B_y^{M_z} B_x^{X_z}})$
Fig. 2a	Supplementary Fig. 2i	Supplementary Fig. 2j	Supplementary Fig. 2k
$E_5 \propto \epsilon_{\alpha\beta\gamma}\omega_\alpha^{M_\alpha} B_\beta^{M_\alpha} B_\gamma^\Gamma$	$E_6 \propto \epsilon_{\alpha\beta\gamma}\omega_\alpha^{M_\alpha} B_\beta^{X_\alpha} B_\gamma^R$	$E_7 \propto \epsilon_{\alpha\beta\gamma}\omega_\alpha^R B_\beta^R A_\gamma^\Gamma$	$E_8 \propto \epsilon_{\alpha\beta\gamma}\omega_\alpha^{M_\alpha} B_\beta^{M_\alpha} A_\gamma^\Gamma$
$(\underline{\omega_z^{M_z} B_x^{M_z} B_y^\Gamma} - \omega_z^{M_z} B_y^{M_z} B_x^\Gamma)$	$(\underline{\omega_z^{M_z} B_x^{X_z} B_y^R} - \omega_z^{M_z} B_y^{X_z} B_x^R)$	$(\underline{\omega_z^R B_x^R A_y^\Gamma} - \omega_z^R B_y^R A_x^\Gamma)$	$(\underline{\omega_z^{M_z} B_x^{M_z} A_y^\Gamma} - \omega_z^{M_z} B_y^{M_z} A_x^\Gamma)$
Fig. 2b and Supplementary Fig. 2b	Supplementary Fig. 2g	Fig. 2a	Fig. 2b and Supplementary Fig. 2a
$E_9 \propto \epsilon_{\alpha\beta\gamma}\omega_\alpha^R B_\beta^{X_\beta} A_\alpha^{M_\beta}$	$E_{10} \propto \epsilon_{\alpha\beta\gamma}\omega_\alpha^R B_\alpha^{X_\beta} A_\alpha^{M_\beta}$	$E_{11} \propto \epsilon_{\alpha\beta\gamma}\omega_\alpha^{M_\alpha} B_\beta^{M_\gamma} A_\alpha^{M_\gamma}$	$E_{12} \propto \epsilon_{\alpha\beta\gamma}\omega_\alpha^{M_\alpha} B_\alpha^{M_\gamma} A_\alpha^{M_\gamma}$
$(\underline{\omega_z^R B_x^{X_x} A_z^{M_x}} - \omega_z^R B_y^{X_y} A_z^{M_y})$	$(\underline{\omega_z^R B_z^{X_x} A_x^{M_x}} - \omega_z^R B_z^{X_y} A_y^{M_y})$	$(\omega_z^{M_z} B_y^{M_x} A_z^{M_y} - \underline{\omega_z^{M_z} B_x^{M_y} A_z^{M_x}})$	$(\omega_z^{M_z} B_z^{M_x} A_y^{M_y} - \underline{\omega_z^{M_z} B_z^{M_y} A_x^{M_x}})$
Supplementary Fig. 2i	Supplementary Fig. 2h	Supplementary Fig. 2d	Supplementary Fig. 2c

The formula of each of these mechanisms is indicated by E_i, with $i=1$–12. Although the summation symbols are omitted, summation for the indices α, β and γ should be done for each E_i. The Levi–Civita symbol $\epsilon_{\alpha\beta\gamma}$, which has a value of $+1$ when $\alpha\beta\gamma$ is xyz, yzx and zxy, -1 when $\alpha\beta\gamma$ is xzy, yxz and zyx, and 0 for cases with repeated indices, is adopted in our formulas. Here, the symbol d_α^K denotes that the displacements are along the α direction for A ($d=A$) or B ($d=B$) ions associated with the K point (for definition, see Supplementary Discussion I). Moreover, we show the expanded forms of these mechanisms (in parentheses) given that ω^M or ω^R is along the z orientation; the underlined terms are sketched and shown in Fig. 1. The DFT results verifying these couplings for tiltings about the z axis are shown in Fig. 2 and Supplementary Fig. 2. For example, the E_1 and E_7 couplings are corroborated by Fig. 2a.
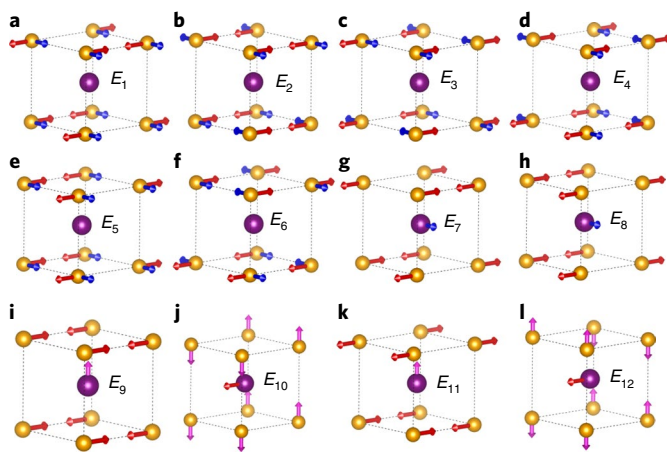

Fig. 1 | Sketches of the atomic motions associated with the 12 trilinear mechanisms. a–l, Atomic motions associated with the underlined E_i ($i=1$–12) terms in Table 1, assuming that the tiltings (not shown in the sketches) are along the z direction. Red, blue and magenta arrows denote motions along the x, y and z directions, respectively; purple and yellow balls denote A and B ions, respectively. For clarity of display, we adopt a cell centred on an A ion.

the unit cell at $\mathbf{R}_{lmn} = l\mathbf{a} + m\mathbf{b} + n\mathbf{c}$ within the considered d sublattice, and N is the total number of lattice sites (the primitive vectors of this lattice are $\mathbf{a}$, $\mathbf{b}$ and $\mathbf{c}$). Similarly, we can define the symmetrized forces $F_\alpha^{K,d}$ of the d sublattice by $F_\alpha^{K,d} = \frac{1}{N}\sum_{lmn} e^{(i\mathbf{K}\cdot\mathbf{R}_{lmn})} F_{lmn,\alpha}^d$, where $F_{lmn,\alpha}^d$ is the α component of the force acting on the ion initially located at $\mathbf{R}_{lmn} = l\mathbf{a} + m\mathbf{b} + n\mathbf{c}$ in the d sublattice. For instance, B_x^R corresponds to displacements of the B ions along the x axis and reverses sign when moving between any two nearest neighbours within the B sublattice; similarly, $A_y^{M_z}$ indicates displacements of A ions along the y direction, which reverse signs between nearest neighbours within the A sublattice inside any xy plane and remain unchanged when moving along the z direction. To further check the validity of these energies, we take BiAlO$_3$ as our platform and perform density functional theory (DFT) calculations to extract ionic forces. For instance, let us start from the cubic phase, and impose a fixed anti-phase tilting of ~8° about the z axis (ω_z^R) for the AlO$_6$ octahedra and create and then vary the strength and sign of the

B_x^R antiferroelectric motions (associated with Al sublattice). These DFT calculations give rise to symmetrized homogeneous (that is, associated with the Γ point) forces along the y axis, acting on Al (denoted by $F_y^{\Gamma,B}$) and Bi (denoted by $F_y^{\Gamma,A}$) sublattices, and linear with B_x^R (Fig. 2a). Such types of forces are precisely those expected from the first and seventh energies shown in Table 1, respectively. Incidentally, this first energy thus indicates that a non-zero and homogeneous y component of the displacement of the B ions can be superimposed on x displacements of the B ions within a G-type antiferroelectricity, and therefore resemble the spin-canted weak ferromagnetism known to coexist with a predominant G-type antiferromagnetism in, for example, rare-earth orthoferrites[30–33]; in this way we can thus begin to demonstrate that there is an electric DMI that is analogous to the magnetic one. Furthermore, we conducted various types of DFT simulations to confirm that all the interaction terms indicated in Table 1 are indeed valid. For instance, Fig. 2b shows that the fifth and eighth terms are applicable, while the relevance of the other energies is revealed in Supplementary Discussion II. We also check our energies based on DFT by fixing the in-phase or anti-phase tiltings to, for example, ~11.3° or ~4.6°. The corresponding DFT results further confirm these energies. Note that the tiltings of ~4.6°, ~8° or ~11.3° are arbitrary choices and have no deeper meaning.

We now check if some of these energies can explain the non-collinear dipole patterns that have been previously documented. The detailed analysis for some examples is shown in Supplementary Discussion III. We noticed that several perovskite oxides (for example, SrTiO$_3$ (ref. [34]), BaMnO$_3$ (ref. [34]), YMnO$_3$ (ref. [34]), BiFeO$_3$ (refs. [34–36]), PbTiO$_3$ (ref. [36]), BiFeO$_3$–PbTiO$_3$ superlattices[36] and rare-earth ferrites[37]) were predicted, via DFT simulations, to exhibit an unusual $Pmc2_1$ phase under tensile strain. This $Pmc2_1$ phase is ferroelectric with a polarization pointing along the pseudo-cubic [110] direction, and also has M_z-point modulated antiferroelectric A and B site ionic motions along the pseudo-cubic [−110] direction, thereby generating an overall zig-zag pattern of cation displacements[35]. It also possesses in-phase tiltings along the z direction ($\omega_z^{M_z}$)[35], as detailed in Supplementary Discussion III. One can easily demonstrate that our E_5, E_8 and E_{14} energies naturally reproduce and thus explain the dipolar patten of the $Pmc2_1$ phase, as shown in Fig. 3a,b. Another example is the experimentally synthesized BiInO$_3$ (ref. [38]) which presents a $Pna2_1$ phase with the following distortions in pseudo-cubic notation: polarization (for example, A_z^Γ), anti-phase tiltings (ω_x^R and ω_y^R) and other distortions such as in-phase tilting
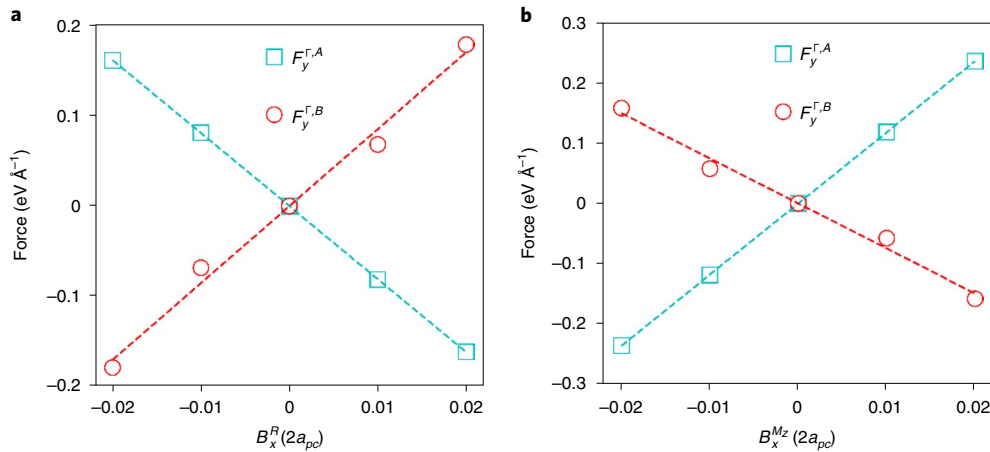
Fig. 2 | Forces acting on Bi and Al ions when displacing, along the x direction, Al ions within R and M_z modulations. a,b, Forces arising from the displacement of Al ions with R (denoted by B_x^R; **a**) and M_z (denoted by $B_x^{M_z}$; **b**) modulations. The anti-phase ω^{R_z} (**a**) and in-phase $\omega_z^{M_z}$ (**b**) tilting about the z axis are fixed at ~8°, and $a_{pc} = 3.82$ Å. The symbol $F_y^{\Gamma,A}$, and $F_y^{\Gamma,B}$ indicates that the measured quantities are symmetrized forces for Bi and Al sublattices, respectively, along y direction associated with the Γ point.
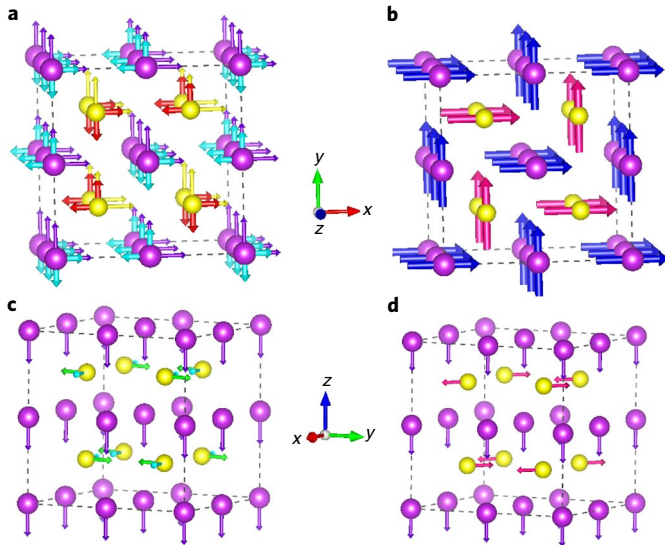

Fig. 3 | Sketches for the ferroelectric and antiferroelectric motions of the A and B ions in ABO_3 perovskites. The motions are represented by arrows, and the A and B ions are denoted by purple and yellow balls, respectively. **a**, A sketch of the couplings of $-\omega_z^{M_z}B_x^{M_z}B_y^\Gamma + \omega_z^{M_z}B_y^{M_z}B_x^\Gamma$ and $\omega_z^{M_z}A_x^\Gamma A_x^{M_z} - \omega_z^{M_z}A_y^\Gamma A_y^{M_z}$; the $(-B_x^{M_z}, B_y^{M_z})$, (B_x^Γ, B_y^Γ), $(A_x^{M_z}, -A_y^{M_z})$ and (A_x^Γ, A_y^Γ) motions are indicated by red, yellow, cyan and purple arrows, respectively. **c**, A sketch of the motion associated with the couplings of $\omega_x^R B_y^R A_z^\Gamma - \omega_y^R B_x^R A_z^\Gamma$; the A_z^Γ and $(B_x^R, -B_y^R)$ motions are indicated by purple and green arrows, respectively. The overall motions for A and B sites resulting from **a** and **c** are displayed in **b** and **d**, respectively, and are consistent with the atomic motions of $Pmc2_1$-phase $BiFeO_3$ and $Pna2_1$-phase $BiInO_3$. In **b**, the magnitude of B^{M_z} and B^Γ are assumed to be identical. Atomic motions associated with octahedral tiltings, $\omega_z^{M_z}$ for $BiFeO_3$ and (ω_x^R, ω_y^R) for $BiInO_3$, are not shown in the sketches.

$(\omega_z^{M_z})$ and anti-polar motions $(A_x^{X_z}, A_y^{X_z}, B_x^{X_z}, B_y^{X_z})$. By symmetry analysis on the experimental crystal structures (see Supplementary Discussion III), we further identified other overlooked anti-polar motions for In ions, that is, B_x^R and B_y^R. The existence of polarization along the z direction (for example, Bi ions) and the R-point modulated anti-polar motions (for example, In ions) along the x

and y directions automatically induce a non-collinear ferroelectricity, which naturally originates from E_7 (see Fig. 3c,d).

The existence of electric DMI

In fact, one can easily show that E_1, E_5, E_7 and E_8 lead to non-collinear ferroelectrics, while the remaining energies in Table 1 result in non-collinear antiferroelectricity. In fact, it is straightforward to demonstrate that the 'non-collinear ferroelectric or antiferroelectric' E_i energies, with $i = 1$–8, essentially have the same form as those recently proposed for non-collinear magnetism (for example, refs. [29,30]), that is:

$$\Delta E_{B,B} \propto \alpha(\boldsymbol{\omega}^R \times \mathbf{R}) \cdot \boldsymbol{\Gamma} + \beta(\boldsymbol{\omega}^R \times \mathbf{M}) \cdot \mathbf{X} \\ + \kappa(\boldsymbol{\omega}^M \times \mathbf{M}) \cdot \boldsymbol{\Gamma} + \lambda(\boldsymbol{\omega}^M \times \mathbf{R}) \cdot \mathbf{X} \tag{1}$$

and

$$\Delta E_{A,B} \propto \gamma(\boldsymbol{\omega}^R \times \mathbf{R}) \cdot \boldsymbol{\Gamma}' + \delta(\boldsymbol{\omega}^M \times \mathbf{M}) \cdot \boldsymbol{\Gamma}' \tag{2}$$

where $\boldsymbol{\omega}^R$, $\boldsymbol{\omega}^M$, $\mathbf{X}$, $\mathbf{M}$, $\mathbf{R}$, $\boldsymbol{\Gamma}$ and $\boldsymbol{\Gamma}'$ represent the vectors having the following Cartesian components $(\omega_x^R, \omega_y^R, \omega_z^R)$, $(\omega_x^{M_x}, \omega_y^{M_y}, \omega_z^{M_z})$, (B_x^X, B_y^X, B_z^X), (B_x^M, B_y^M, B_z^M), (B_x^R, B_y^R, B_z^R), $(B_x^\Gamma, B_y^\Gamma, B_z^\Gamma)$ and $(A_x^\Gamma, A_y^\Gamma, A_z^\Gamma)$, respectively. Note that the (B_x^X, B_y^X, B_z^X) or (B_x^M, B_y^M, B_z^M) are in fact $(B_x^{X_u}, B_y^{X_v}, B_z^{X_w})$ or $(B_x^{M_u}, B_y^{M_v}, B_z^{M_w})$ (u, v and w being x, y or z), respectively, with X_u and M_v interpreted in the following ways: for the κ, δ and λ terms, both u and v in $B_p^{X_u}$ or $B_q^{M_v}$ component coupled with $\omega_j^{M_i}$ should be equal to i; for the β term, the u and v should always be identical.

Note that all the aforementioned terms in equations (1) and (2) involve long-range-ordered vectors such as the in-phase tilting $(\boldsymbol{\omega}^M = (\omega_x^{M_x}, \omega_y^{M_y}, \omega_z^{M_z})$ with $\omega_x^{M_x} = \sum_{lmn}(-1)^{(m+n)}\omega_{lmn,x}/N$, $\omega_y^{M_y} = \sum_{lmn}(-1)^{(l+n)}\omega_{lmn,y}/N$ and $\omega_z^{M_z} = \sum_{lmn}(-1)^{(l+m)}\omega_{lmn,z}/N)$, anti-phase tilting $(\boldsymbol{\omega}^R = \sum_{lmn}(-1)^{(l+m+n)}\boldsymbol{\omega}_{lmn}/N)$, ferroelectric motions $(\boldsymbol{\Gamma}, \boldsymbol{\Gamma}')$ and antiferroelectric motions $(\mathbf{X}, \mathbf{M}, \mathbf{R})$; these terms give us the possible origin of electric DMI in perovskites and can be used in investigations based on phenomenological theory. Also, the α, κ, λ, γ and δ terms correspond to E_1, E_5, E_6, E_7 and E_8 in Table 1, respectively; the β term is the compact way of including E_2, E_3 and E_4 simultaneously. The extension of the magnetic DMI, coupling $\mathbf{S}_i$ and $\mathbf{S}_j$ by $\mathbf{D}_{ij} \cdot (\mathbf{S}_i \times \mathbf{S}_j)$ and
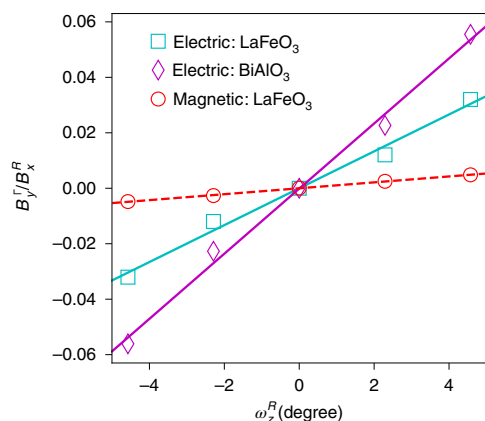
Fig. 4 | The renormalized weak magnetic and/or ferroelectric components of LaFeO₃ and BiAlO₃ as a function of anti-phase tiltings ω_z^R. The weak magnetic components are renormalized to the predominant antiferromagnetic components of Fe (~4.0 μ_B), while the weak ferroelectric components are renormalized with respect to the predominant antiferroelectric component imposed on Fe or Al (0.04a_{pc}, in Å). The results for LaFeO₃ and BiAlO₃ are based on LDA and PBEsol functionals, respectively. The slopes (linear fitting) for the cyan square, purple diamond and red circle symbols are 0.0067, 0.012 and 0.001 per degree, respectively, with coefficients of determination of 0.989, 0.994 and 0.999.

responsible for some non-collinear magnetism via the dependency of $\mathbf{D}_{ij}$ on oxygen octahedral tiltings proposed in refs. [29,30], can thus naturally be extended to ferroelectrics and related systems. In other words, an electric DMI coupling the i- and j-site displacement pairs by $\mathbf{D}'_{ij} \cdot (\mathbf{u}_i \times \mathbf{u}_j)$, for which $\mathbf{D}'_{ij}$ is dependent on oxygen octahedral tiltings as well, indeed exists. Moreover, and as detailed in Supplementary Discussion IV, it is straightforward to use the E_i energies, with $i = 1$–12, to determine the explicit dependence of the DMI coefficients, $\mathbf{D}'_{ij}$, on anti-phase and in-phase tiltings for $B−B$ and $A−B$ pairs in perovskites.

One-to-one correspondence between magnetic and electric DMIs
Let us now solely consider symmetry. A detailed analysis in Supplementary Discussion V shows that the $\mathbf{S}_i \times \mathbf{S}_j$ and $\mathbf{u}_i \times \mathbf{u}_j$ transform identically under all symmetry elements of three-dimensional Euclidean space and of course the symmetry elements of space groups of crystals, because the latter is a subset of the former. Consequently, $\mathbf{D}_{ij} \cdot (\mathbf{S}_i \times \mathbf{S}_j)$ and $\mathbf{D}'_{ij} \cdot (\mathbf{u}_i \times \mathbf{u}_j)$ are both allowed by symmetry; one-to-one correspondence between magnetic and electric DMIs can be established (Supplementary Discussion V). As a result, any DMI-based phenomenological theory that is valid for magnetism should also be transferrable to electric systems and vice versa. Note that this conclusion is also technically valid even if $\mathbf{D}_{ij}$ and $\mathbf{D}'_{ij}$ do not explicitly depend on oxygen octahedral tiltings, which are hypothetical cases not considered above. Indeed, our DFT results and the symmetry analysis detailed above for perovskites show that electric DMI can originate from the existence of oxygen octahedral tiltings and their trilinear interactions with different possible cationic modes, but symmetry arguments do not prevent other quantities from also generating electric DMI. For example, we have examined one possible mechanism for electric DMI without involving tiltings but involving electric polarization (Supplementary Discussion VI), and discovered a polarization-driven electric DMI that is the counterpart of the magnetic DMI based on a spin–current model[39]. On the other hand, the microscopic origin for magnetic and electric DMIs are, of course, completely different. Indeed, the former stems from

spin–orbit coupling whereas the latter does not. A definite proof is that we obtained non-collinear (anti)ferroelectricity by performing first-principles simulations without having to include spin–orbit coupling. It is noteworthy that both the electric and magnetic DMIs structurally stem from the distortions (for example, tiltings and polarization) in the same manner as seen from our above analysis. It is interesting to extract the strengths of the electric and magnetic DMIs from their effects (for example, dipole and spin cantings). We thus employ LaFeO₃ and BiAlO₃ to make such a comparison. Starting from the cubic phases (of LaFeO₃ and BiAlO₃), we impose a sequence of z-oriented anti-phase tiltings with various magnitudes, and create the R-point modulated predominant antiferroelectric or antiferromagnetic vectors along the x direction (denoted by B_x^R); then we perform structural relaxations or non-collinear magnetism calculations, and obtain the weak ferroelectric motion or weak magnetism along the y direction (denoted by B_y^Γ) for each configuration with specified anti-phase tilting. The electric and magnetic versions of B_y^Γ / B_x^R—which quantify the dipole and spin cantings (for example, $\tan\theta = B_y^\Gamma / B_x^R$, where θ is the canting angle)—as a function of ω_z^R are shown in Fig. 4. Interestingly, the dipole cantings can be much larger than spin cantings in magnitude, reflecting that the electric D'/J' (D' and J' being the electric DMI and the exchange interaction) can be much stronger than its magnetic counterpart. See Supplementary Discussion VII for detailed discussion.

Other mechanisms for non-collinear dipole patterns
Finally, it is worth emphasizing that the electric DMI is not the only mechanism creating non-collinear dipole patterns. For instance, there are six additional couplings in the form of $\sum_{\alpha\beta\gamma} \epsilon_{\alpha\beta\gamma} \omega_\alpha Q_{1,\beta} Q_{2,\beta}$ (α, $\beta = x$, y, z, $\alpha \neq \beta$), shown in Supplementary Table II and Supplementary Discussion III and IV, with none of them implying a DMI because the Q_1 and Q_2 modes are along the same direction (Supplementary Table II)—while they can host non-collinear ferroelectricity or antiferroelectricity in some special cases. For example, the z-oriented $\omega_z^{M_z}$ and xy-oriented B^Γ mode (for example, (B_x^Γ, B_y^Γ)) imply the $x\bar{y}$-oriented A^{M_z} mode (for example, $(A_x^{M_z}, -A_y^{M_z})$), constituting non-collinear ferroelectricity (see the E_{15} term in Supplementary Table II). Moreover, in $Pbnm$ ABO_3 perovskites with both in-phase and anti-phase BO_6 tiltings (for example, $\omega_z^{M_z}$, ω_{xy}^R), there are two kinds of A-site anti-polar motions (that is, $A_{xy}^{X_z}$ and $A_{\bar{x}y}^R$) sourced from $\omega_{xy}^R \omega_z^{M_z} A_{xy}^{X_z}$ and $\omega_{xy}^R \omega_z^{M_z} \omega_z^{M_z} A_{\bar{x}y}^R$, respectively[40]. This leads to another kind of non-collinear antiferroelectricity which does not depend on the electric DMI either. Similarly, if we create polarization by forming hybrid improper ferroelectricity in, for example, $A'BO_3/A''BO_3$ superlattices[41–45], we then obtain non-collinear ferroelectricity that is not related to an electric DMI. In fact, non-collinear electric dipole patterns can also appear in nanostructures due to effects that are different from DMI. One example is the Bloch components in the 180° domain wall of PbTiO₃, as predicted by second- and first-principles simulations[46,47]. In fact, these Bloch components, arising from a symmetry-breaking phase transition at the domain wall, do not rely on the electric DMI but are rather due to the spatial deviation of polarization (for example, $(\nabla\mathbf{P})^2$, from the viewpoint of phenomenological theory)[48] or Pb–O hybridization at the domain wall (from the viewpoint of chemical bonding)[47]. Similarly, the recently proposed electric skyrmion/bubbles in PbTiO₃ are partly formed as a result of these Bloch components[49]. Meanwhile, the mixed Bloch/Néel-type electric bubble domains (seen as the precursor of electric skyrmions) found in ref. [24] mostly rely on the depolarizing field and not at all on electric DMI.

Perspective
Our findings clearly support the existence of an electric DMI and reveal the one-to-one correspondence between it and its magnetic

counterpart. As a result, the present work enables the generalization between magnetic and electric theories as long as these theories are rooted in the DMI. Furthermore, we anticipate that various magnetic-DMI-related phenomena will probably find their equivalent parts for electric systems. We thus hope that this article opens or deepens the field of DMIs in systems possessing dipoles. In particular, by comparing with magnetic cases, ref. [28] proposed the existence of electric Bloch skyrmions due to $\mathbf{u} \cdot (\nabla \times \mathbf{u})$ (where $\mathbf{u}$ is the displacement). Similarly, symmetry arguments also imply the occurrence of $u_z(\nabla \cdot \mathbf{u}) - (\mathbf{u} \cdot \nabla)u_z$, which can create, in principle, electric Néel skyrmions (Supplementary Discussion V). It will be interesting to determine if electric skyrmions based on these two mechanisms of the electric DMI can be discovered in real materials.

Online content

References

1. Dzyaloshinskii, I. E. Thermodynamic theory of 'weak' ferromagnetism in antiferromagnetic substances. *Sov. Phys. JETP* **5**, 1259–1266 (1957).
2. Moriya, T. Anisotropic superexchange interaction and weak ferromagnetism. *Phys. Rev.* **120**, 91–98 (1960).
3. Heinze, S. et al. Spontaneous atomic-scale magnetic skyrmion lattice in two dimensions. *Nat. Phys.* **7**, 713–718 (2011).
4. Wiesendanger, R. Nanoscale magnetic skyrmions in metallic films and multilayers: a new twist for spintronics. *Nat. Rev. Mater.* **1**, 16044 (2016).
5. Bera, S. & Mandal, S. S. Theory of the skyrmion, meron, antiskyrmion, and antimeron in chiral magnets. *Phys. Rev. Res.* **1**, 033109 (2019).
6. Im, M.-Y. et al. Symmetry breaking in the formation of magnetic vortex states in a permalloy nanodisk. *Nat. Commun.* **3**, 983 (2012).
7. Kwon, H. Y., Kang, S. P., Wu, Y. Z. & Won, C. Magnetic vortex generated by Dzyaloshinskii–Moriya interaction. *J. Appl. Phys.* **113**, 133911 (2013).
8. Pereiro, M. et al. Topological excitations in a kagome magnet. *Nat. Commun.* **5**, 4815 (2014).
9. Gao, N. et al. Creation and annihilation of topological meron pairs in in-plane magnetized films. *Nat. Commun.* **10**, 5603 (2019).
10. Ishikuro, Y., Kawaguchi, M., Kato, N., Lau, Y.-C. & Hayashi, M. Dzyaloshinskii–Moriya interaction and spin–orbit torque at the Ir/Co interface. *Phys. Rev. B* **99**, 134421 (2019).
11. Dong, S., Xiang, H. & Dagotto, E. Magnetoelectricity in multiferroics: a theoretical perspective. *Natl. Sci. Rev.* **6**, 629–641 (2019).
12. Dong, S., Liu, J.-M., Cheong, S.-W. & Ren, Z. Multiferroic materials and magnetoelectric physics: symmetry, entanglement, excitation, and topology. *Adv. Phys.* **64**, 519–626 (2015).
13. Dubovik, V. & Tugushev, V. Toroid moments in electrodynamics and solid-state physics. *Phys. Rep.* **187**, 145–202 (1990).
14. Lin, L.-F., Zhang, Y., Moreo, A., Dagotto, E. & Dong, S. Frustrated dipole order induces noncollinear proper ferrielectricity in two dimensions. *Phys. Rev. Lett.* **123**, 067601 (2019).
15. Prosandeev, S., Malashevich, A., Raevski, I. P. & Bellaiche, L. Dynamical magnetoelectric effects associated with ferroelectric domain walls. *Phys. Rev. B* **91**, 100101 (2015).
16. Prosandeev, S. et al. Natural optical activity and its control by electric field in electrotoroidic systems. *Phys. Rev. B* **87**, 195111 (2013).
17. Prosandeev, S., Ponomareva, I., Naumov, I., Kornev, I. & Bellaiche, L. Original properties of dipole vortices in zero-dimensional ferroelectrics. *J. Phys. Condens. Matter* **20**, 193201 (2008).
18. Prosandeev, S., Kornev, I. & Bellaiche, L. Tensors in ferroelectric nanoparticles: first-principles-based simulations. *Phys. Rev. B* **76**, 012101 (2007).
19. Nahas, Y. et al. Discovery of stable skyrmionic state in ferroelectric nanocomposites. *Nat. Commun.* **6**, 8542 (2015).
20. Lu, L. et al. Topological defects with distinct dipole configurations in PbTiO₃/SrTiO₃ multilayer films. *Phys. Rev. Lett.* **120**, 177601 (2018).
21. Yadav, A. K. et al. Observation of polar vortices in oxide superlattices. *Nature* **530**, 198–201 (2016).
22. Jia, C.-L., Urban, K. W., Alexe, M., Hesse, D. & Vrejoiu, I. Direct observation of continuous electric dipole rotation in flux-closure domains in ferroelectric Pb(Zr,Ti)O₃. *Science* **331**, 1420–1423 (2011).
23. Nelson, C. T. et al. Spontaneous vortex nanodomain arrays at ferroelectric heterointerfaces. *Nano Lett.* **11**, 828–834 (2011).
24. Zhang, Q. et al. Nanoscale bubble domains and topological transitions in ultrathin ferroelectric films. *Adv. Mater.* **29**, 1702375 (2017).
25. Das, S. et al. Observation of room-temperature polar skyrmions. *Nature* **568**, 368–372 (2019).
26. Prosandeev, S. et al. In *Nanoscale Ferroelectrics and Multiferroics* (eds Algueró, M. et al.) 700–728 (John Wiley, 2016).
27. Naumov, I. I., Bellaiche, L. & Fu, H. Unusual phase transitions in ferroelectric nanodisks and nanorods. *Nature* **432**, 737–740 (2004).
28. Erb, K. C. & Hlinka, J. Vector, bidirector, and Bloch skyrmion phases induced by structural crystallographic symmetry breaking. *Phys. Rev. B* **102**, 024110 (2020).
29. Bellaiche, L., Gui, Z. & Kornev, I. A. A simple law governing coupled magnetic orders in perovskites. *J. Phys. Condens. Matter* **24**, 312201 (2012).
30. Zhao, H. J., Íñiguez, J., Chen, X. M. & Bellaiche, L. Origin of the magnetization and compensation temperature in rare-earth orthoferrites and orthochromates. *Phys. Rev. B* **93**, 014417 (2016).
31. White, R. L. Review of recent work on the magnetic and spectroscopic properties of the rare-earth orthoferrites. *J. Appl. Phys.* **40**, 1061–1069 (1969).
32. Bousquet, E. & Cano, A. Non-collinear magnetism in multiferroic perovskites. *J. Phys. Condens. Matter* **28**, 123001 (2016).
33. Zhao, H. J., Ren, W., Yang, Y., Chen, X. M. & Bellaiche, L. Effect of chemical and hydrostatic pressures on structural and magnetic properties of rare-earth orthoferrites: a first-principles study. *J. Phys. Condens. Matter* **25**, 466002 (2013).
34. Varignon, J., Bristowe, N. C. & Ghosez, P. Electric field control of Jahn–Teller distortions in bulk perovskites. *Phys. Rev. Lett.* **116**, 057602 (2016).
35. Yang, Y., Ren, W., Stengel, M., Yan, X. H. & Bellaiche, L. Revisiting properties of ferroelectric and multiferroic thin films under tensile strain from first principles. *Phys. Rev. Lett.* **109**, 057602 (2012).
36. Yang, Y., Stengel, M., Ren, W., Yan, X. H. & Bellaiche, L. Epitaxial short-period PbTiO₃/BiFeO₃ superlattices studied by first-principles calculations. *Phys. Rev. B* **86**, 144114 (2012).
37. Zhao, H. J. et al. Creating multiferroics with large tunable electrical polarization from paraelectric rare-earth orthoferrites. *J. Phys.: Condens. Matter* **26**, 472201 (2014).
38. Belik, A. A., Stefanovich, S. Y., Lazoryak, B. I. & Takayama-Muromachi, E. BiInO₃: a polar oxide with GdFeO₃-type perovskite structure. *Chem. Mater.* **18**, 1964–1968 (2006).
39. Katsura, H., Nagaosa, N. & Balatsky, A. V. Spin current and magnetoelectric effect in noncollinear magnets. *Phys. Rev. Lett.* **95**, 057205 (2005).
40. Bellaiche, L. & Íñiguez, J. Universal collaborative couplings between oxygen-octahedral rotations and antiferroelectric distortions in perovskites. *Phys. Rev. B* **88**, 014104 (2013).
41. Bousquet, E. et al. Improper ferroelectricity in perovskite oxide artificial superlattices. *Nature* **452**, 732–736 (2008).
42. Benedek, N. A. & Fennie, C. J. Hybrid improper ferroelectricity: a mechanism for controllable polarization–magnetization coupling. *Phys. Rev. Lett.* **106**, 107204 (2011).
43. Mulder, A. T., Benedek, N. A., Rondinelli, J. M. & Fennie, C. J. Turning ABO₃ antiferroelectrics into ferroelectrics: design rules for practical rotation-driven ferroelectricity in double perovskites and A₃B₂O₇ Ruddlesden–Popper compounds. *Adv. Funct. Mater.* **23**, 4810–4820 (2013).
44. Rondinelli, J. M. & Fennie, C. J. Octahedral rotation-induced ferroelectricity in cation ordered perovskites. *Adv. Mater.* **24**, 1961–1968 (2012).
45. Zhao, H. J., Íñiguez, J., Ren, W., Chen, X. M. & Bellaiche, L. Atomistic theory of hybrid improper ferroelectricity in perovskites. *Phys. Rev. B* **89**, 174101 (2014).
46. Wojdeł, J. C. & Íñiguez, J. Ferroelectric transitions at ferroelectric domain walls found from first principles. *Phys. Rev. Lett.* **112**, 247603 (2014).
47. Wang, Y. J., Chen, D., Tang, Y. L., Zhu, Y. L. & Ma, X. L. Origin of the Bloch-type polarization components at the 180° domain walls in ferroelectric PbTiO₃. *J. Appl. Phys.* **116**, 224105 (2014).
48. Hlinka, J. & Márton, P. Phenomenological model of a 90° domain wall in BaTiO₃-type ferroelectrics. *Phys. Rev. B* **74**, 104104 (2006).
49. Gonçalves, M. A. P., Escorihuela-Sayalero, C., Garca-Fernández, P., Junquera, J. & Íñiguez, J. Theoretical guidelines to create and tune electric skyrmion bubbles. *Sci. Adv.* **5**, eaau7023 (2019).

Methods

We employ the VASP code[50,51] to perform first-principles simulations with the PBEsol functional[52] based on the projector augmented wave[53], taking $BiAlO_3$ as a model system. In particular, we work with a 40-atom supercell ($2 \times 2 \times 2$), solving ($5d$, $6s$, $6p$) electrons for Bi, ($3s$, $3p$) for Al and ($2s$, $2p$) for O, with $E_{cut} = 500$ eV and a k-point mesh of $6 \times 6 \times 6$. We start from the cubic perovskite $BiAlO_3$ with $Pm\bar{3}m$ symmetry (lattice parameter $a = 2a_{pc} = 7.64$ Å, where a_{pc} is the pseudo-cubic lattice constant), impose anti-phase or in-phase tiltings for AlO_6 octahedra, displace the Bi or Al ions in some distortion modes, and then compute and analyse the forces on the Bi and Al ions. The energetic coupling terms are derived by group-theoretical-based symmetry analysis[54] with the help of the Bilbao Crystallographic Server (https://www.cryst.ehu.es); such couplings are reproduced by the L-INVARIANT code (https://github.com/PaulChern/LINVARIANT/) based on Mathematica software (https://www.wolfram.com/mathematica) with the help of ISOTROPY Software Suite (https://stokes.byu.edu/iso/isotropy.php). Some of the figures are prepared by using VESTA[55], Matplotlib[56] and Mathematica as well. Regarding Supplementary Discussion VII, we solve the following electronic configurations by VASP: ($5p$, $5d$, $6s$) for La, ($3p$, $3d$, $4s$) for Fe and ($2s$, $2p$) for O within the framework of the local density approximation functional[57]. In particular, we use the local density approximation functional to achieve a good convergence for the calculations of non-collinear magnetism. Also, a Hubbard U correction[58] with an effective U value of 4.0 eV is carried out for the $3d$ electrons of Fe. To further save computational time, in non-collinear magnetism calculations, a relatively coarse but still sufficiently dense k-point mesh of $4 \times 4 \times 4$ was used.

Data availability

All the data (for example, raw data and Matplotlib-based scripts for analysing and visualizing the data) supporting the present work are available from the corresponding author upon request. Please note that our data figures were prepared with the use of some Matplotlib-based scripts (for example, with some mathematical processes such as post-processing of the data or fitting inside the scripts). Consequently, we prefer to share our raw data as well as the scripts to interested readers on request, so that we can help them in case of need. We do not upload our data and scripts because the latter may depend on the version of Python.

Code availability

The VASP code for the numerical simulations in this work can be found at https://www.vasp.at; the code L-INVARIANT can be found at https://github.com/PaulChern/LINVARIANT/; the Mathematica software is available at https://www.wolfram.com/mathematica; the Matplotlib is available at https://matplotlib.org; other codes and scripts can be obtained on request from the corresponding author.

References

50. Kresse, G. & Furthmüller, J. Efficient iterative schemes for ab initio total-energy calculations using a plane-wave basis set. *Phys. Rev. B* **54**, 11169–11186 (1996).
51. Kresse, G. & Joubert, D. From ultrasoft pseudopotentials to the projector augmented-wave method. *Phys. Rev. B* **59**, 1758–1775 (1999).
52. Csonka, G. I. et al. Assessing the performance of recent density functionals for bulk solids. *Phys. Rev. B* **79**, 155107 (2009).
53. Blöchl, P. E. Projector augmented-wave method. *Phys. Rev. B* **50**, 17953–17979 (1994).
54. Koster, G. F., Dimmock, J. D., Wheeler, R. G. & Statz, H. *Properties of the Thirty-Two Point Group* (MIT Press, 1963).
55. Momma, K. & Izumi, F. VESTA3 for three-dimensional visualization of crystal, volumetric and morphology data. *J. Appl. Crystal.* **44**, 1272–1276 (2011).
56. Hunter, J. D. Matplotlib: a 2D graphics environment. *Comput. Sci. Eng.* **9**, 90–95 (2007).
57. Ceperley, D. M. & Alder, B. J. Ground state of the electron gas by a stochastic method. *Phys. Rev. Lett.* **45**, 566–569 (1980).
58. Dudarev, S. L., Botton, G. A., Savrasov, S. Y., Humphreys, C. J. & Sutton, A. P. Electron-energy-loss spectra and the structural stability of nickel oxide: an LSDA+U study. *Phys. Rev. B* **57**, 1505–1509 (1998).

Acknowledgements

Author contributions

L.B. and H.J.Z. conceived the work. H.J.Z. performed the DFT simulations. H.J.Z., P.C., S.P. and S.A. carried out symmetry analysis. All authors participated in the discussion and preparation of this work.

Competing interests

The authors declare no competing interests.

Additional information

Supplementary information is available for this paper at https://doi.org/10.1038/s41563-020-00821-3.

Correspondence and requests for materials should be addressed to P.C. or L.B.

Reprints and permissions information is available at www.nature.com/reprints.